

Globular Clusters GMRT Pulsar Search (GCGPS) I: Survey description, discovery and timing of the first pulsar in NGC 6093 (M80)

JYOTIRMOY DAS ¹, JAYANTA ROY ¹, PAULO C. C. FREIRE ², SCOTT M RANSOM ³, BHASWATI BHATTACHARYYA ¹,
KAREL ADÁMEK ⁴, WES ARMOUR ⁴, SANJAY KUDALE ^{1,5} AND MEKHALA V. MULEY ⁵

¹*National Center for Radio Astrophysics (NCRA)
Pune-411007, Maharashtra, India*

²*Max-Planck-Institut für Radioastronomie (MPIfR)
Auf dem Hügel 69-53121, Bonn, Germany*

³*National Radio Astronomy Observatory (NRAO)
Charlottesville, Virginia, United States*

⁴*Oxford e-Research Center (OeRC) University of Oxford, Oxford-OX13PJ, United Kingdom*

⁵*Giant Metrewave Radio Telescope (GMRT)
Khodad, Pune- 410504, Maharashtra, India*

ABSTRACT

This paper describes the new Globular Clusters GMRT Pulsar Search (GCGPS) survey. This survey aims to find MSPs in the globular clusters (GCs) of the Milky Way using uGMRT. The observations use the uGMRT’s Band-4 (550–750 MHz) and Band-3 (300–500 MHz) receivers, which are well suited for steep-spectral-index radio sources like MSPs; the survey will eventually cover the GCs accessible to the uGMRT sky (i.e. $\delta > \sim -53^\circ$), and that is South of $\delta = -17^\circ$ (FAST sky limit) and have not been targeted with the sensitivity of this survey. The observations started in May 2023, having so far resulted in seven new discoveries. In this paper, we present the discovery and follow-up study of the first pulsar from this survey, J1617–2258A, a 4.32 ms binary MSP that is also the first to be discovered in the globular cluster NGC 6093. We localised this MSP with arc-sec precision from imaging and obtained the unique timing solution from more than one year of timing observations with the Band-4 (550–750 MHz) receivers of the uGMRT. This revealed an unusual binary MSP, with a ~ 19 -hour, highly eccentric ($e \sim 0.54$) orbit having a low-mass companion. This orbital eccentricity allowed the measurement of the rate of advance of periastron for this system, which led to the derivation of its total mass, $1.67 \pm 0.06 M_\odot$; this together with the system’s mass function implies, for the pulsar and the companion, $M_p < 1.60 M_\odot$ and $M_c > 0.072 M_\odot$. The system is likely a perturbed MSP - Helium WD system seen at a low orbital inclination.

Keywords: Radio astronomy; LMXBs; Pulsar survey: GCGPS; Globular clusters: NGC 6093; Pulsar: J1617–2258A

1. INTRODUCTION

The close interaction of an old neutron star (NS) with a low-mass star results in the formation of low-mass X-ray-binaries (LMXBs). In such systems, the NS accretes matter from its companion star and gradually spins up. The high stellar density and high stellar interaction rates (Verbunt & Hut 1987; Pooley et al. 2003; Bahramian et al. 2013) found in globular clusters allow for the dynamical formation of LMXBs, which is not possible in the Galactic disk, this is the reason why there are $\sim 10^3$ times more LMXBs per unit mass in GCs compared to the Galactic disk (Sarazin et al.

2003). At the end of the dynamical evolution of these LMXBs, we are left with pulsars with spin periods of a few milliseconds, called recycled or millisecond pulsars (MSP, defined here as having $P < 20$ ms and a low B-field, Becker & Trümper 1999), and a low-mass non-degenerate companion or a low-mass white-dwarf (for a review, see Tauris & van den Heuvel 2023). The large number of LMXBs results in a large number of MSPs: out of the 729 discovered MSPs, 311 are found in glob-

ular clusters¹, where LMXBs are many orders of magnitude more abundant per unit of stellar mass than in the Galactic disk.

The local environment of a globular cluster plays an important role, not only in the formation of LMXBs and MSPs but also afterwards. If the stellar interaction rate per binary, γ (Verbunt & Freire 2014) is not very high, the evolution from an LMXB to an MSP is likely to be undisturbed and we are likely to get a spider MSP or an NS-WD binary, which is therefore indistinguishable from the MSPs in the galactic disc, as observed in lower density GCs, like M3 (Li et al. 2024), M5 (Zhang et al. 2023), M13 (Wang et al. 2020) and M53 (Lian et al. 2023, 2025). If γ is very high, then LMXBs might be disrupted to form exotic MSPs, where the end of the accretion results in the formation of mildly recycled, high-B field MSPs (Freire et al. 2011; Johnson et al. 2013). But even after the accretion ends, interaction with a third stellar object may lead either to the dissociation of binary systems and the isolation of many pulsars, as observed in core-collapsed GCs like Terzan 1 (Singleton et al. 2024), NGC 6517 (Lynch et al. 2011; Yin et al. 2024), NGC 6522 (Abbate et al. 2023), NGC 6624 (Lynch et al. 2012; Abbate et al. 2022), NGC 6752 (Corongiu et al. 2024) and M15 (Zhou et al. 2024; Wu et al. 2024) or to an exchange of the companion of an MSP (generally for a more massive one) in what has been designated as a *secondary exchange* (e.g. PSR J1807–2500B in NGC 6544 Lynch et al. 2012, PSR J1823–3021G in NGC 6624, Ridolfi et al. 2021 and PSR J1835–3259A in NGC 6652, DeCesar et al. 2015). For GCs with intermediate densities, like NGC 1851 (Freire et al. 2004; Ridolfi et al. 2022a), Terzan 5 (Ransom et al. 2005; Padmanabh et al. 2024) and M28 (Bogdanov et al. 2011; Douglas et al. 2022), we see a mix of both types of populations. Interestingly, some reasonably dense GCs like 47 Tuc (Freire et al. 2017) or M62 (Vleschower et al. 2024) show a “normal” MSP population, only truncated in the orbital period.

The large eccentricities and companion masses of some of the exotic systems make them potentially useful probes of gravitational effects in strong field regimes: for instance, NGC 1851E might be an MSP-black hole system (Barr et al. 2024), which would enable tests of new types of gravity theories that until now could not be tested with binary pulsar timing (Freire & Wex 2024). Such unusual systems provide a strong motivation for finding additional pulsars in GCs.

Because typical GC distances are of the order of tens of kiloparsecs (kpc), most pulsars, which are generally faint radio sources, remain undetected. Indeed, Galactic disk MSPs are typically found within distances of the order of a kpc. This implies two things: 1) the vast majority of GC pulsars remain undetected, meaning many more pulsars in GCs are yet to be discovered; 2) discovering them will require more sensitive surveys.

Most of the successful and most recent surveys have been conducted in the GHz frequency range, either in L-Band, like Parkes and Arecibo GC surveys (carried out around 2000, Camilo et al. 2000; Possenti et al. 2001, 2005; D’Amico et al. 2003; Hessels et al. 2007), the ongoing Transients and Pulsars with MeerKAT (TRAPUM Ridolfi et al. 2021, 2022a) and FAST (Pan et al. 2021a,b) surveys or in S-Band, like the GBT S-Band GC Pulsar Survey (see Ransom et al. 2004, 2005; Freire et al. 2008; Lynch et al. 2011, see also discussion in Section 2); this means that such surveys are biased towards relatively flat-spectrum MSPs. The advent of the upgraded Giant Metrewave Radio Telescope (uGMRT) and its unique seamless low-frequency coverage (300–850 MHz for uGMRT Band-3 and Band-4) allowed us to use its unique Y-shaped array and effectively design a pulsar survey to search for GC MSPs in the low-frequency range. Searching GC MSPs with the uGMRT will allow us to discover steep spectrum GC MSPs that may have been missed earlier due to bias towards flat spectrum MSPs of surveys at higher frequencies.

In this paper, we discuss the Globular Clusters GMRT Pulsar Search (GCGPS), from its motivation (Section 2) to its design, sensitivity, and target selection in Section 3. In Section 4, a detailed discussion is done on the strategy of data analysis. In Section 5.1 we report the first GCGPS discovery, a pulsar in the globular cluster NGC 6093 (also known as Messier 80, henceforth M80), followed by its localization in Section 5.2, profile study in Section 5.3, timing in Section 5.4 followed by its binary properties in Section 5.5 and finally we summarize our work in Section 6.

2. MOTIVATION FOR DESIGNING AN GC MSP SEARCH SURVEY WITH THE UGMRT

The improvement in sensitivity achieved with the uGMRT relative to the legacy GMRT implies the possibility of additional pulsar discoveries. Furthermore, the large number of undiscovered pulsars in GCs and the possibility of finding exotic binaries there, that are unlike the Galactic disk pulsars serve as the motivation for this survey.

There are two previously reported GC MSP discoveries with GMRT. A survey of 10 GCs was made with

¹ Data taken from the ATNF Pulsar catalogue (<https://www.atnf.csiro.au/research/pulsar/psrcat/>) and Paulo Freire’s GC website (<https://www3.mpifr-bonn.mpg.de/staff/pfreire/GCpsr.html>).

the legacy GMRT, which resulted in the discovery of the first MSP in NGC 1851, PSR J0514–4002A, a steep spectrum 5-ms pulsar that is a member of one of the first exotic binaries known that was clearly formed in a secondary exchange encounter (Freire et al. 2004). The most recent effort was a shallow survey made by Gautam et al. (2022), where they discovered the second MSP of NGC 6652, PSR J1835–3259B, an exceptionally young, powerful and radio bright system that has a bright, young WD companion (Chen et al. 2023) and is one of the three GC pulsars detected in γ -rays (Zhang et al. 2022). These surveys, but especially the latter, take full advantage of the imaging capabilities of the uGMRT, which have uncovered additional candidates, both in pulsation and imaging data.

One crucial factor about the existing and ongoing searches of pulsars from the GCs is that they mostly focus on the GCs that have discovered pulsars in them, as the known DM reduces the computational requirements. MeerKAT’s TRAPUM and the uGMRT survey by Gautam et al. (2022) followed this strategy. Because of this several GCs with no discovered MSPs remained unobserved by sensitive surveys like MeerKAT’s TRAPUM or uGMRT; even though some of the GCs were previously observed by GBT or Parkes, those observations were mostly in GHz frequency (Ransom et al. 2004, 2005; Possenti et al. 2005) and were significantly less sensitive compared to uGMRT Band-4 (550–750 MHz) central square phased array beam sensitivity for same on-source time (discussed in Section 3.3), for steep spectrum pulsars. uGMRT’s unique low-frequency (300–850 MHz for uGMRT Band-3 and Band-4) coverage makes those remaining GCs very optimistic targets to search for new MSPs that may have never been searched or missed by earlier high-frequency surveys.

Due to FAST and MeerKAT’s superior sensitivity (quantified in Section 3.3), the GCs that remained unobserved by FAST’s GC MSP search (L-Band), or MeerKAT’s TRAPUM (UHF and L-Band survey), make a good set of GCs to design an effective survey to search for MSPs with uGMRT. After careful consideration, we got a significant number of such observable GCs and the majority of them met our additional selection criteria (discussed in Section 3.3), which motivated us to design the GCGPS² survey.

3. THE SURVEY

² Survey webpage: <http://www.ncra.tifr.res.in/~jroy/GC.html>

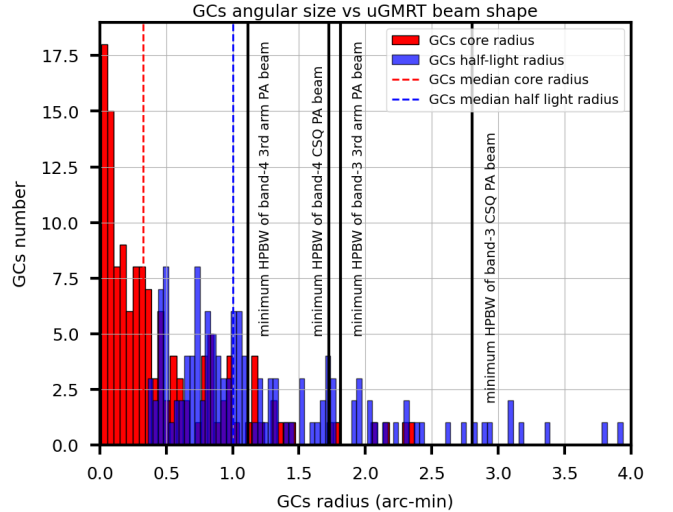


Figure 1. Histogram plot of all the globular clusters (GCs) core and half-light radius. The vertically dotted red line represents the median core radius value and the similar blue line represents the median half-light radius of all the GCs. All the GC data was taken from W. E. Harris’s GC catalogue (Harris 1996, 2010 edition). The four vertical solid black lines represent the uGMRT Band-3 and Band-4, CSQ and 3rd arm PA beam’s minimum Half Power Bandwidth ($HPBW_{min}$), as marked in the plot.

In this section, we will discuss the GCGPS survey details, from strategic design to the theoretical estimation of the survey sensitivity and target selection.

3.1. Designing the survey

The uGMRT has 30 antennae distributed in a Y-shaped fashion, with a compact array of 14 antennae at the centre within a 1 km^2 area, and the other 16 antennae are distributed in the three arms with a maximum baseline length of $\sim 28 \text{ km}$ to make the array suitable to observe the compact objects (Swarup et al. 1991; Gupta et al. 2017).

To design this GC MSP search survey effectively for uGMRT, we need to have an initial estimation of the typical target size for this survey. The core and half-light radius distribution (Figure 1) of all the Milky Way GCs have a median core and half-light radius of 0.325 and 1.0 arcminutes, respectively³. With this initial estimation, to select our optimal uGMRT observing Band and beam type, using a uGMRT beam simulation code `uGMRT_beam_fov.py`⁴ developed for the SPOTLIGHT⁵

³ Data from W. E. Harris list of GC parameters, (Harris 1996, 2010 edition), <https://physics.mcmaster.ca/~harris/mwgc.dat>

⁴ See https://www.ursi.org/proceedings/RCRS/2024/RCRS2024_0897.pdf

⁵ SPOTLIGHT survey webpage: <https://spotlight.ncra.tifr.res.in/>

project, we simulated several types of uGMRT beams and their size variation as a function of elevation for uGMRT Band-3 and Band-4 on NGC 6093 as a reference GC.

Based on the beam simulation results keeping a balance between sensitivity and sky coverage the uGMRT Band-3 and Band-4 central square’s (CSQ) phased array (PA) beams were the most suitable bands and primary beam type for designing the survey. A PA beam is formed by adding all the antenna voltages coherently preserving the phase information, making the beam narrower but more sensitive than an incoherent array (IA) beam (PA beam sensitivity is \sqrt{N} times IA beam sensitivity, where N is the number of antennae used to form the beam) that is formed by incoherently adding all the antenna power without the phase information. A CSQ PA beam is a PA beam that is formed only using the closely packed (within 1 km²) 14 uGMRT central square (CSQ) antennas, which are wider than the PA beams formed by adding the long-spaced arm antennas.

Statistically, as illustrated in Figure 1, the minimum Half Power Bandwidth (HPBW) of the Band-4 PA beam exceeds the half-light radius for 77% of GCs, while for Band-3, it does so for 92%. We expect to find our MSPs close to the core of the GC. In the observed MSP distribution (as shown in Figure 2), 96% of all the reported localized GC MSPs have a positional offset⁶ from the GC centre that is less than the minimum HPBW of uGMRT CSQ Band-4 PA beam and 86% for them have offset value less than HPBW/2 (indicating they are residing in the GC core region). This result is not a selection effect: in most surveys - especially the Parkes and GBT surveys, and the Arecibo searches at lower frequencies - the search beams’ HPBWs are larger than 4 arcminutes. For Band-3, this coverage is even better, statistically establishing that to observe the whole target GC with optimized sensitivity, Band-3 or Band-4 CSQ PA beam is sufficient.

Between Band-3 and Band-4, we preferred Band-4 as the first choice due to its lower system temperature (for 650 MHz, $T_{\text{sys}} \sim 102.5$ K) compared to Band-3 (for 400 MHz, $T_{\text{sys}} \sim 130$ K, reference [Gautam et al. \(2022\)](#)). Additionally, Band-4 experiences significantly less Radio Frequency Interference (RFI), making it the cleanest Band of the uGMRT, whereas Band-3 is more adversely affected by RFI. We use Band-3 only when the target is significantly wider, as it provides better sensitivity coverage compared to Band-4. We excluded Band-5 due to

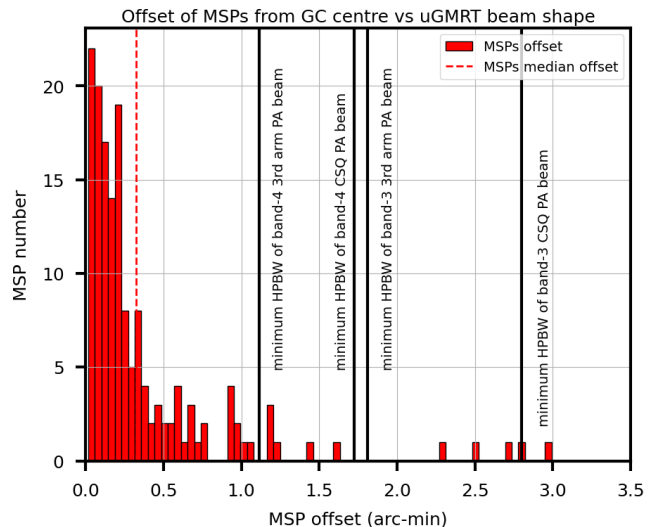


Figure 2. Histogram of the reported position offsets of all GC MSPs from the cluster centre. The back solid lines are the same as Figure 1

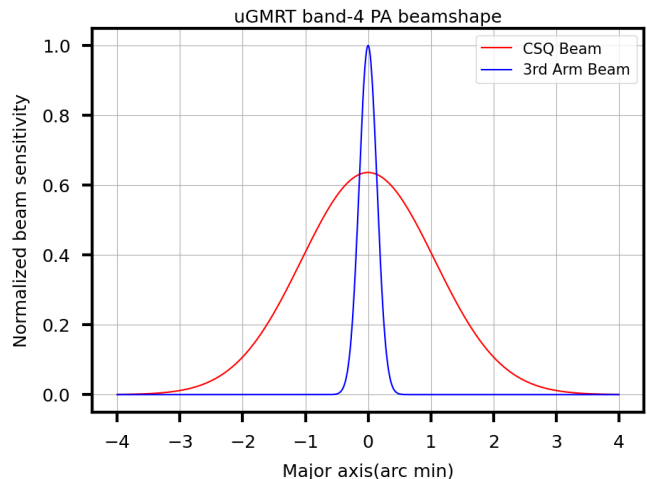


Figure 3. The uGMRT Band-4 CSQ and 3rd arm PA beam’s major axis (calculated using `uGMRT_beam_fov.py` for the same initial condition) versus normalised beam sensitivity (to 3rd arm PA beam sensitivity), where it is assumed that the beam sensitivity response is a Gaussian response.

its reduced gain, narrower beam size compared to Band-3 and Band-4 and its focus on high-frequency coverage (where, as discussed in Section 2, low-frequency coverage is preferred).

Along with covering the whole GC with optimum sensitivity, to observe the core with even better sensitivity (where we expect most of our MSPs will be, as we see in Figure 2), we decided to simultaneously form another PA beam including up to the third antenna in each arm (i.e. $N = 22$) called the 3rd arm PA beam. As we can see in Figure 3, due to differences in the baseline length and the number of antennas, the sensitivity of the 3rd

⁶ All the MSP position offset data taken from Paulo Freire GC website, see: <https://www3.mpifr-bonn.mpg.de/staff/pfreire/GCpsr.html>

arm PA beam is higher than that of the CSQ PA beam (theoretically: number of 3rd arm antennas/number of CSQ antennas = 22/14 \sim 1.6 times). However, the CSQ beam exhibits a wider response compared to the 3rd arm beam. As shown in Figure 1, the uGMRT Band-4 (our primary observing Band) CSQ PA beam’s minimum HPBW is larger than the half-light radius for approximately 77% of GCs, enabling full coverage of the GC with optimal sensitivity. Similarly, for the 3rd arm PA beam, around 87% of GCs have their core radius within the minimum HPBW, providing optimal coverage of the GC core.

An additional advantage of observing a GC simultaneously with two beams (CSQ and 3rd arm) is that, upon detecting a pulsar in the beam data, the SNR ratio between the two beams can immediately provide an estimate of the pulsar’s positional offset from the cluster centre, using the known beam response from our simulation code. For a pulsar sitting exactly in the beam centre, as discussed earlier we would expect the 3rd arm beam SNR will be \sim 1.6 times higher than the CSQ beam SNR and this factor will decrease systematically (as shown in Figure 3) with a systematic increase of the position offset from the beam centre. With an initial offset estimation, follow-up imaging observations can accurately localise the pulsar in the image plane (see Section 5.2) with minimal effort.

To meet our sensitivity criteria (discussed in Section 3.2) we decided to spend 2.5 hours of observing time on each target. Before the target scan, the entire array is phased on a calibrator to form the PA beam. To maintain the PA beam’s sensitivity during the extended 2.5-hour target scans, interleaved phasing is required. Instrumental and ionospheric phase perturbations necessitate intermediate phasing every 45 minutes, resulting in two phasing sessions over a 2.5-hour duration. This intermediate phasing allowed us to preserve the PA beam sensitivity eliminating the array de-phasing sensitivity loss for 2.5 hours of continuous recording.

3.2. Observation strategy and sensitivity coverage

In GCGPS we primarily used uGMRT Band-4 (550–750 MHz) and for a few wider targets Band-3 (300–500 MHz) as discussed in Section 3.1. For a specific Band, the observation strategies employed to achieve optimal target sensitivity are discussed along with the theoretical sensitivity coverage. Given that we are searching for MSPs at mid and low frequencies (with a median GC MSP spin period of 4.60 ms⁷), the sensi-

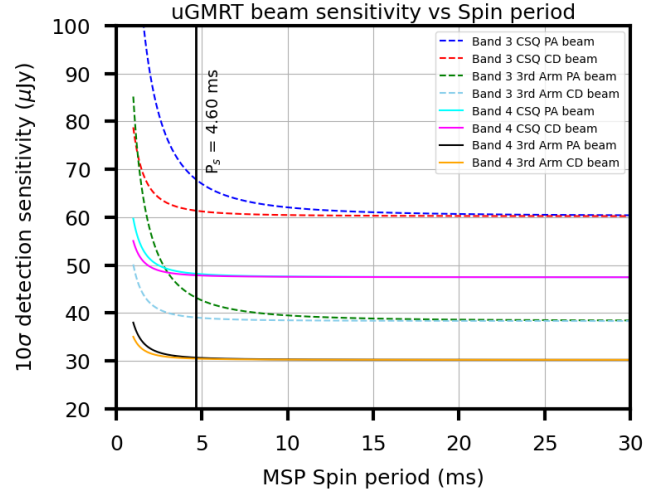


Figure 4. The uGMRT 10σ detection sensitivity (in μJy) versus the spin period of the observed pulsar for all the observing modes and bands for the GCGPS. The sensitivity is calculated using the radiometer equation (refer to Equation 3) for a pulsar with 10% duty cycle assuming a DM value of 50 pc cm^{-3} . The black vertical line represents the sensitivity achieved for pulsar with the median spin period of all the GC MSPs.

tivity loss due to pulse broadening from scattering and intra-channel dispersion becomes significant.

According to Bhat et al. (2004), the scatter broadening W_{scatt} in ms is defined as,

$$\log[W_{\text{scatt}}] = -6.46 + 0.154 \log[DM] + 1.07 \log[DM]^2 - 3.86 \log[\nu], \quad (1)$$

where DM is the dispersion measure in pc cm^{-3} and ν is the observing frequency in GHz.

According to Lorimer & Kramer (2004) the smearing (W_{DM}) due to intra-channel dispersion can be defined as,

$$W_{\text{DM}} = 8.3 \times DM \times \frac{\Delta\nu}{\nu^3} \mu\text{s}, \quad (2)$$

here $\Delta\nu$ is the channel width/resolution in MHz and ν is the observing frequency in GHz.

While scattering is unavoidable in low-frequency observations, intra-channel dispersion can be eliminated by recording the data in coherently de-dispersed (CD) mode (see Hankins (1971)), provided the GC’s DM is precisely known beforehand. By mitigating intra-channel dispersion smearing, this mode enables the recording of high-time-resolution data by reducing the frequency channels in the filterbank output.

The GCs targeted in GCGPS primarily lack known pulsars (as discussed in Section 2), with only a few containing a minimal number of MSPs (discussed in Section 3.3). For GCs with precisely known DM (have

⁷ Data taken from: <https://www3.mpifr-bonn.mpg.de/staff/pfreire/GCpsr.html>

discovered MSPs), we observe it with two (CSQ and 3rd arm) simultaneously recorded CD beams (coherently dedispersed at the GC MSPs' median DM) having 512 channels and 40.96 μs sampling time. For GCs with no known DM, we record two (CSQ and 3rd arm) PA beams with 4096 channels and 81.92 μs sampling time.

For each observing mode, the theoretical sensitivity limit can be calculated using the radiometer equation (Dewey et al. 1985). The minimum detectable flux (S_{\min}) is defined as:

$$S_{\min} = \frac{SNRT_{\text{sys}}\beta}{GN\sqrt{n_{\text{pol}}BW\Delta t_{\text{obs}}}}\sqrt{\frac{W_{\text{eff}}}{P_s - W_{\text{eff}}}} \quad (3)$$

We define S_{\min} as 10σ (i.e. $SNR = 10$) detection flux. For 8-bit recording, we assume the digitization loss (β) to be ~ 1 . For Band-3 at 400 MHz, $T_{\text{sys}} \sim 130\text{ K}$, where for Band-4 at 650 MHz, $T_{\text{sys}} \sim 102.5\text{ K}$ as mentioned earlier in Section 3.1. For uGMRT, the gain per antenna (G) is about 0.35 KJy^{-1} . As discussed above, $N = 14$ for CSQ and 22 for the 3rd arm PA beams. For total intensity Stokes-I data, the number of polarizations (n_{pol}) summed up is 2. Our on-source time (Δt_{obs}) is 2.5 hours for each beamforming observation per target. For Band-3 and Band-4, after eliminating the periodic narrow-band RFI-affected channels, the effective Bandwidth (BW) is about 150 MHz and 180 MHz respectively.

Now the effective pulse width can be defined as:

$$W_{\text{eff}} = \sqrt{W_{\text{int}}^2 + W_{\text{DM}}^2 + W_{\text{scatt}}^2 + t_{\text{samp}}^2} \quad (4)$$

where, W_{int} is the intrinsic pulse width, and t_{samp} is the smearing that rises due to finite sampling time. W_{scatt} and W_{DM} (defined in Equation 1 and 2) are the intra-channel dispersion smearing and scatter broadening time-scale respectively. For CD recording $W_{\text{DM}} = 0$ and $t_{\text{samp}} = 40.96\mu\text{s}$ whereas for PA data W_{DM} have a finite value according to Equation 2 and $t_{\text{samp}} = 81.92\mu\text{s}$. For both PA and CD, W_{scatt} is the same and calculated using Equation 1, where for uGMRT Band-3 and Band-4 ν is 0.40 GHz, and 0.65 GHz respectively.

For sensitivity analysis, we use intrinsic pulse width (W_{int}) as 10% of the pulse period (P_s) and $DM = 50\text{ pc cm}^{-3}$, which is a reasonable estimation for a low-frequency MSP survey like the GCGPS. Figure 4 illustrates that the most sensitive survey beam for GCGPS is the uGMRT Band-4 3rd arm CD beam, which is closely matched in sensitivity to the PA beam of the same Band and antenna configuration.

We present the theoretical 10σ detection flux for the GCGPS survey for different observation modes for a 4.60 ms MSP (median spin period of all GC pulsars) with a

DM value of 50 pc cm^{-3} in Table 1. Figure 4 shows the detection sensitivity for all the GCGPS observing modes as a function of pulsar spin period (P_s).

3.3. Target selection

As discussed in Section 2, currently the most prominent ongoing GC search surveys are MeerKAT's TRAPUM and FAST's GC survey. According to Ridolfi et al. (2022a), for 2 hours of on-source time, the minimum detectable flux (10σ) is 14 μJy and 10 μJy for MeerKAT's UHF (544–1087 MHz) and L-Band (856–1711 MHz) respectively. Whereas according to Pan et al. (2021a), for FAST's L-Band(1.0 GHz-1.5 GHz) survey it's 0.76 μJy (same on-source time and detection limit). Assuming the pulsar spectral index -2 , the TRAPUM's L-Bands (the most used Band) scaled sensitivity at 650 MHz (uGMRT Band-4) is about $\sim 39\mu\text{Jy}$, and for FAST it's about 2.81 μJy . Now from Ridolfi et al. (2022b), for the same on source time (2 hours), duty cycle (8%), DM (52 pc cm^{-3}) and assuming the pulsar period about 10 ms, the GCGPS primary beam's (Band-4 CSQ PA beam) theoretical 10σ sensitivity limit is about 36 μJy .

As the FAST GC project follows observing GCs independent of the fact of having discovered MSPs in them or not, along with its superior sensitivity compared to the GCGPS survey, we completely excluded the FAST sky (i.e. $\delta > -17^\circ$) for our survey. Also, due to the comparable sensitivity of MeerKAT's TRAPUM for pulsars having a high spectral index, we exclude the GCs that have already been observed by MeerKAT. Now the remaining GCs were the GCs in the sky $-53^\circ < \delta < -17^\circ$ ($\delta > -53^\circ$, is the uGMRT sky coverage to have at least 2 hours of target on-source time), and not observed under TRAPUM project.

Most of the remaining GCs had no prior reported MSP search observations, while a subset had been previously observed with the GBT's 2 GHz survey or Parkes' 1.4 GHz GC survey. Assuming an MSP spectral index of -2 (with GBT 2 GHz and Parkes 1.4 GHz sensitivities scaled to uGMRT Band-4 at 650 GHz), for the same on-source time the theoretical sensitivity of GCGPS is approximately 3 times better than that of GBT and about 8 times better than the Parkes survey. Therefore, we considered observations of the GBT and Parkes observed GCs in the GCGPS (uGMRT Band-3 and Band-4) frequencies.

Figure 5 illustrates significant sensitivity loss in both Band-3 and Band-4 due to intra-channel dispersion and scattering at higher DMs. However, Band-4 maintains moderate sensitivity even at higher DMs, which was one of the key reasons for selecting it as our primary observing band over Band-3. To account for this sensitivity

Table 1. Sensitivity estimation of GCGPS survey using the Radiometer equation by Dewey et al. (1985), for all the GCGPS observing modes and bands with typical on-source time per target. The presented estimated sensitivity is calculated for the median spin period of all the GC MSPs (median $P_s = 4.60$ ms), for a DM value of 50 pc cm^{-3} with a duty cycle of 10%.

On-source time (hours)	Spin period (ms)	uGMRT Band (Band-3/Band-4)	uGMRT array (CSQ/3rd arm)	Beam type (PA/CD)	Sampling (μs)	Channel (number)	$S_{min}(10\sigma)$ (μJy)
2.5	4.60	Band-3	CSQ	PA	81.92	4096	68
				CD	40.96	512	61
			3rd arm	PA	81.92	4096	43
				CD	40.96	512	39
		Band-4	CSQ	PA	81.92	4096	48
				CD	40.96	512	47
			3rd arm	PA	81.92	4096	30
				CD	40.96	512	30

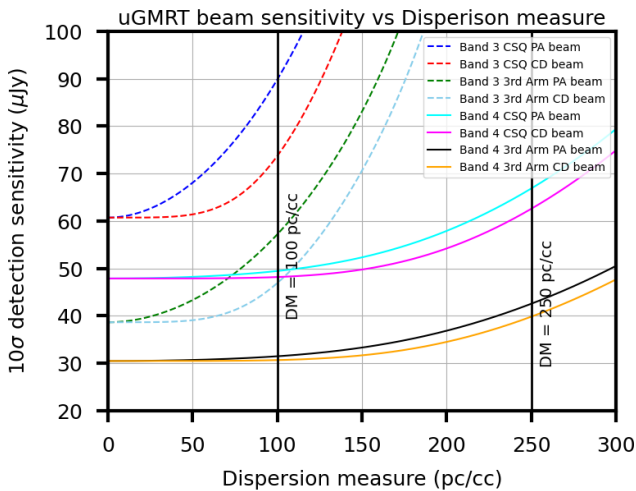


Figure 5. Plot representing the uGMRT 10σ detection sensitivity versus DM variation for a fixed pulsar period and duty cycle of 4.60 ms (median spin period of all GC MSPs) and 10% respectively, for all the GCGPS observing modes and Bands in different colours. The two vertical black lines represent the effect of DM on detection significance for values of 100 pc cm^{-3} and 250 pc cm^{-3} respectively.

loss, from the remaining GCs, we chose targets with known or predicted maximum DMs of $\sim 250 \text{ pc cm}^{-3}$ for Band-4. For broader targets requiring Band-3 observations, the maximum DM (known or predicted) was limited to less than 100 pc cm^{-3} . We also note that the scatter-broadening timescale predicted by Equation 1 does not account for the possibility that GCs, being located at higher Galactic latitudes, may experience reduced scattering even for distant sources with higher DMs. This results in shorter scattering timescales observed for GC pulsars compared to field pulsars with equivalent DMs (He & Shi 2024). This will result in sensitivity loss even lower than the value we got using Equation 1, 2, 3, and 4.

Finally, as the MSPs can be a prominent source of X-ray/gamma-ray emissions (Freire et al. 2011; Johnson et al. 2013; Zhang & Cheng 2003; Zhang et al. 2022), we ranked the GCs based on reported X-ray/gamma-ray brightness from different high-energy surveys (Webb et al. 2006; Abdo et al. 2010; Tam et al. 2011, 2016). Globular clusters without any discovered pulsars but exhibiting very high gamma-ray brightness are ideal targets for our survey. Compactness and higher total mass were also considered to prioritise the GC observations. We also assigned lower priority to GCs located more than ~ 15 kiloparsecs (kpc) away or with a half-light radius exceeding twice the HPBW of the uGMRT CSQ PA beam. After applying these criteria, 31 GCs were identified as optimal candidates for the GCGPS survey. In Table 2, we present these 31 GCs with their relevant information, which will be observed (over multiple uGMRT cycles) under GCGPS using the uGMRT Band-4 CSQ PA beam as the primary observing mode.

We note that we are planning to include the globular clusters (GCs) observed with MeerKAT in our survey in the near future. This will be facilitated by the improved sensitivity and sky-coverage offered by the multi-beam formation using the full uGMRT array, utilizing all 30 antennas instead of the single-beam formation by the 14 antennae, which is currently in use in GCGPS. The key enabler of this enhancement is the SPOTLIGHT backend⁸, which allows target-specific multi-beam formation with a maximum of 200 post-correlation beams^{9,10}. Additionally, we will deploy the in-field phasing technique

⁸ For relevant information about the SPOTLIGHT project, see <https://spotlight.ncra.tifr.res.in/>

⁹ See <https://www.ursi.org/proceedings/R CRS/2024/R CRS2024-0803.pdf>

¹⁰ See <https://www.ursi.org/proceedings/R CRS/2024/R CRS2024-1101.pdf>

Table 2. The list of GCs observed so far under the GCGPS survey. All these GCs met our selection criteria to make a good set to search for MSPs using uGMRT. All the relevant values were taken from the W. E. Harris list of GC parameters, (Harris 1996, 2010 edition). The DM values in the last column of the table either represent the median DM of all the MSPs in that particular GC (GCs with already known MSPs), or the YMW16 model (Yao et al. 2017) predicted DMs (the DMs marked with “*”), for GCs with no discovered pulsars.

GC name (NGC XXXX)	RA (J2000) (hh mm ss)	Dec (J2000) (dd mm ss)	Core radius (arc-min)	Half-light radius (arc-min)	Distance from sun (kpc)	GC DM (pc cm ⁻³)
NGC 1904	05 24 11.09	-24 31 29.0	0.16	0.65	12.9	53.1*
NGC 4590	12 39 27.98	-26 44 38.6	0.58	1.51	10.3	50.3*
NGC 5286	13 46 26.81	-51 22 27.3	0.28	0.73	11.7	146.3*
NGC 5897	15 17 24.50	-21 00 37.0	1.40	2.06	12.5	48.6*
NGC 5986	15 46 03.00	-37 47 11.1	0.47	0.98	10.4	92.17
NGC 6093	16 17 02.41	-22 58 33.9	0.15	0.61	10.0	75.2*
NGC 6121	16 23 35.22	-26 31 32.7	1.16	4.33	2.2	62.86
NGC 6139	16 27 40.37	-38 50 55.5	0.15	0.85	10.1	166.6*
NGC 6273	17 02 37.80	-26 16 04.7	0.43	1.32	8.8	125.9*
NGC 6284	17 04 28.51	-24 45 53.5	0.07	0.66	15.3	142.5*
NGC 6287	17 05 09.13	-22 42 30.1	0.29	0.74	9.4	115.4*
NGC 6293	17 10 10.20	-26 34 55.5	0.05	0.89	9.5	146.4*
NGC 6304	17 14 32.25	-29 27 43.3	0.21	1.42	5.9	153.3*
NGC 6316	17 16 37.30	-28 08 24.4	0.17	0.65	10.4	186.1*
NGC 6333	17 19 11.26	-18 30 57.4	0.45	0.96	7.9	114.2*
NGC 6342	17 21 10.08	-19 35 14.7	0.05	0.73	8.5	122.4*
NGC 6355	17 23 58.59	-26 21 12.3	0.05	0.88	9.2	182.6*
NGC 6356	17 23 34.93	-17 48 46.9	0.24	0.81	15.1	144.4*
NGC 6388	17 36 17.23	-44 44 07.8	0.12	0.52	9.9	171.4*
NGC 6528	18 04 49.64	-30 03 22.6	0.13	0.38	7.9	206.9*
NGC 6541	18 08 02.36	-43 42 53.6	0.18	1.06	7.5	108.4*
NGC 6553	18 09 17.60	-25 54 31.3	0.53	1.03	6.0	227.3*
NGC 6569	18 13 38.80	-31 49 36.8	0.35	0.80	10.9	175.7*
NGC 6637	18 31 23.10	-32 20 53.1	0.33	0.84	8.8	119.8*
NGC 6638	18 30 56.10	-25 29 50.9	0.22	0.51	9.4	155.5*
NGC 6642	18 31 54.10	-23 28 30.7	0.10	0.73	8.1	155.8*
NGC 6652	18 35 45.63	-32 59 26.6	0.10	0.48	10.0	116.6*
NGC 6681	18 43 12.76	-32 17 31.6	0.03	0.71	9.0	105.2*
NGC 6717	18 55 06.04	-22 42 05.3	0.08	0.68	7.1	103.3*
NGC 6723	18 59 33.15	-36 37 56.1	0.83	1.53	8.7	82.0*
NGC 6809	19 39 59.71	-30 57 53.1	1.80	2.83	5.4	56.7*

developed by Kudale et al. (2024), ensuring that the highly sensitive PA beam (formed using all 30 antennas) maintains its sensitivity over long on-source time. These advancements will enhance our survey sensitivity by a factor of 2–3 for uGMRT Band-3 and Band-4, compared to the current sensitivity of the GCGPS.

This will enable us to observe all low-DM GCs ($DM < 250 \text{ pc cm}^{-3}$) seamlessly within the declination range $-53^\circ < \delta < -17^\circ$.

In this paper, we present the discovery of the first MSP in NGC 6093 from the GCGPS, along with its timing studies. A comprehensive list of already GCGPS observed GCs from Table 2, including all discoveries and non-detection limits, will be detailed in future publications.

4. DATA ANALYSIS

The PA beam data recorded from the uGMRT GWB backend (Reddy et al. 2017) was initially processed to mitigate RFI signals and to correct instrumental effects, such as slopes in the bandpass. We used GPTOOL¹¹ to eliminate RFI signals exceeding the threshold value along both the time and frequency axes, as well as to normalise the Band shape. The Bandpass-corrected filtered beam data was then converted to the SIGPROC¹² filterbank format for further processing. We developed an end-to-end PRESTO¹³-based pulsar search pipeline called PulsarSearchScript (*PSS*), which is available on GitHub¹⁴. This pipeline is integrated with a candidate sifting code, enabling the reduction of the huge number of candidates (based on some thresholds and grouping criteria discussed below) to search for MSPs efficiently. We used the GHRSS (Bhattacharyya et al. 2016, 2019) survey discovered MSPs’ data to test and optimise this code for the GCGPS.

To begin the search for any periodic signals, the data must first be de-dispersed. For the observed GCs that already had discovered pulsars, we searched within a range of the median $DM \pm 15 \text{ pc cm}^{-3}$ with a DM step of 0.02 pc cm^{-3} , resulting in a total of 1500 DM trials. After de-dispersion, we performed a Fast Fourier Transform (FFT) on the de-dispersed data, followed by an acceleration search with a $\pm 200(z_{\text{max}})$ bin drift correction to account for the doppler-shifted period caused by the line-of-sight (LOS) acceleration of a binary system.

After the acceleration search, to reduce the huge number of candidates we apply a DM clustering filter in

our candidate sifting code. The optimisation of the sifting code led us to assume that our lowest period MSP should be present in a DM space of 0.3 pc cm^{-3} before getting undetectable due to dispersion, making the sifting code sensitive towards finding faint MSPs while eliminating redundant and spurious candidates efficiently. This along with the search DM step determines our DM clustering threshold. For the GCs with known MSPs (i.e. known DMs), as we search with the DM step of 0.02 pc cm^{-3} , the clustering threshold becomes 15 ($0.3/0.02$). We also apply a periodicity range and a minimum σ threshold (threshold equivalent to SNR) to filter candidates within our region of interest. For the general search, the candidate σ cutoff was set to 5, and the periodicity range was limited to up to 10 seconds. After this sifting, we were left with a manageable number of candidates, which we folded over frequency and time domains using PRESTO’s `prepfold`. Then manual inspections were conducted over these folded profiles to check for the presence of any periodic signals in both time and frequency domains.

To process the data from GCs without any discovered pulsars, we initially used both the NE2001 (Cordes & Lazio 2002) and YMW16 (Yao et al. 2017) models to predict the GC DM and optimise our DM search range. Testing both models on GCs with known DMs revealed that both tend to overpredict the GC DM at the given GC distance. However, in most cases, the YMW16 model provided DM predictions closer to the actual values compared to the NE2001 model. In the worst-case scenario, the YMW16 model predicted DM was a factor of 1.5–2 higher than the GC DM. This observation led us to use the YMW16 model over the NE2001 to predict the DM values for further analysis.

Using the predicted DM value (DM^*), we searched over the DM space as given below (optimising computational cost):

$$\frac{1}{3}DM^* \leq DM \leq \frac{3}{2}DM^*, \quad (5)$$

or

$$DM = DM^* \pm 50 \text{ pc cm}^{-3} \quad (6)$$

We chose our DM space according to Equation 5 or Equation 6, whichever probes a larger DM range. As shown in Equation 5, for larger predicted DM values, the DM search range is biased towards lower DMs rather than higher DMs due to the overpredictive nature of the YMW16 model. For GCs with no pulsars, we have used a DM step of 0.1 pc cm^{-3} for optimising the computational costs. After dedispersion, we applied the same approach as discussed earlier. We processed the data through PSS using this DM plan, applying a clustering

¹¹ See <https://github.com/chowdhuryaditya/gptool>

¹² See <https://sigproc.sourceforge.net/>

¹³ PRESTO GitHub page: <https://github.com/scottransom/presto>

¹⁴ See <https://github.com/jyotirmoydas5392/PulsarSearchScript>

DM cutoff of 3 DM steps (with a DM step is 0.1 pc cm^{-3} , the clustering cutoff becomes $0.3/0.1 = 3$, as discussed earlier), the candidate σ cutoff of 5σ and period cutoff of 10 seconds like earlier, to reduce the number of candidates. This was followed by folding the filtered candidates and performing the manual inspection for any presence of periodic signals in time and frequency space. The described search strategies were systematically applied to process all of our GCGPS data.

5. FIRST PULSAR DETECTED IN NGC 6093 (M80)

5.1. *Discovery*

Under GCGPS, in July 2023 we observed NGC 6093, using uGMRT Band-4 CSQ and 3rd arm PA beams simultaneously. At first, we performed the search on the CSQ data having wider beam response, using the YMW16 predicted value for NGC 6093 ($DM^* \sim 75.2 \text{ pc cm}^{-3}$), following Equation 6 over the DM range of 25 to 125 pc cm^{-3} , with DM step 0.1 pc cm^{-3} . During the manual inspection of the folded profiles in the search output, we identified an MSP at a period of 4.32 ms with a DM of 66.9 pc cm^{-3} . With 2.5 hours of on-source time, the CSQ beam resulted in a detection SNR of 16.3σ , whereas the 3rd arm beam folding for this MSP (with the known period, period derivative and DM a priori from CSQ detection) yielded a detection significance of 6.3σ . This difference in SNR suggests a positional offset of the MSP from the cluster centre (details in Section 5.2). In this region, the sensitivity of the 3rd arm beam decreases rapidly, whereas the wider CSQ beam maintains moderate sensitivity, allowing better coverage. In Figure 6, we present the discovery folded profile plot of J1617–2258A (the first pulsar of M80, henceforth J1617–2258A), from the standard PRESTO folding output.

5.2. *Localization*

In the GCGPS observations, simultaneous to the beam recording we also record the interferometric data with a time integration of 5.3 sec for imaging analysis of the field. The imaging is done using the automated pipeline, called CAPTURE (Kale & Ishwara-Chandra 2021) developed for the uGMRT data. For the M80 observations, we observed 3C48 as the amplitude calibrator and 1830–360 was observed for every 40 minutes of the target scan (scan of NGC 6093) as a phase calibrator.

The uGMRT interferometric imaging for 2.2 hours of integration time on M80, resulted in an rms noise of $\sim 20 \mu\text{Jy}$. Imaging of the field revealed 4 sources within a 1.5 arc-min radius from the cluster centre. The first source (the source visible in Figure 7) was $\sim 6.5''$ off from the cluster centre where the discovery beam was

formed. During discovery observation, the detection significance for the CSQ PA beam was 16.3σ , whereas for the 3rd Arm PA beam the detection significance was 6.3σ . The approximate distance of the source was calculated using the SNR ratio of both the beams and the beam simulation code `uGMRT_beam_fov.py` (see Section 3.1). We simulated the Band-4 CSQ and the 3rd Arm PA beam for the time of observation to determine the offset from the beam centre. The simulation indicates that the source is located within approximately 10 arc-seconds of the cluster centre. Now the source with a $\sim 6.5''$ off from the cluster centre, and an imaging estimated flux of $350 \pm 25 \mu\text{Jy}$ was considered as the primary target as the position of the pulsar.

To verify this position estimate, we observed NGC 6093 using both the CSQ and 3rd Arm PA beams, centred on the probable pulsar location (i.e. $\sim 6.5''$ off from the cluster centre). For 1.5 hours of on-source time, the CSQ and 3rd Arm PA beam detection significance was 12.2σ and 17.3σ respectively. According to the radiometer equation (for reference Figure 3), assuming the pulsar is sitting in the beam centre, the expected 3rd arm SNR is ~ 1.6 times CSQ SNR and our obtained SNR ratio value is ~ 1.42 ($17.3/12/2$). We note that the theoretical and observed SNR ratio difference may arise due to multiple factors like the phasing efficiency, available antennas, RFI condition for both beams, etc. Therefore, we identified this radio source as J1617–2258A and proceeded with timing follow-up to enhance astrometric precision.

More than one year of timing follow-up of J1617–2258A allowed us to obtain a phase-coherent timing solution (discussed in Section 5.4), improving the positional error (1σ) up to $0.30''$. The timing position is marked in Figure 7 with the letter “A”, which overlaps with the imaging position, confirming that it is J1617–2258A.

5.3. *Scattering timescale and profile evolution*

We observed J1617–2258A in Band-4 ($f_c = 650 \text{ MHz}$) CD (coherently dedispersed) mode (with $10.24 \mu\text{s}$ sampling and 512 channels) along with the default PA mode of $81.92 \mu\text{s}$ and 4096 channels, to obtain a pulse profile unaffected by intra-channel dedispersion. We also observed J1617–2258A in uGMRT Band-3 ($f_c = 400 \text{ MHz}$) with coherent dedispersion (at $40.96 \mu\text{s}$ sampling and 1024 channels) to probe its profile evolution in lower frequencies. We utilised the coherently dedispersed pulse profiles from Band-4 and Band-3 to characterise the low-frequency profile evolution and determine the scattering timescale.

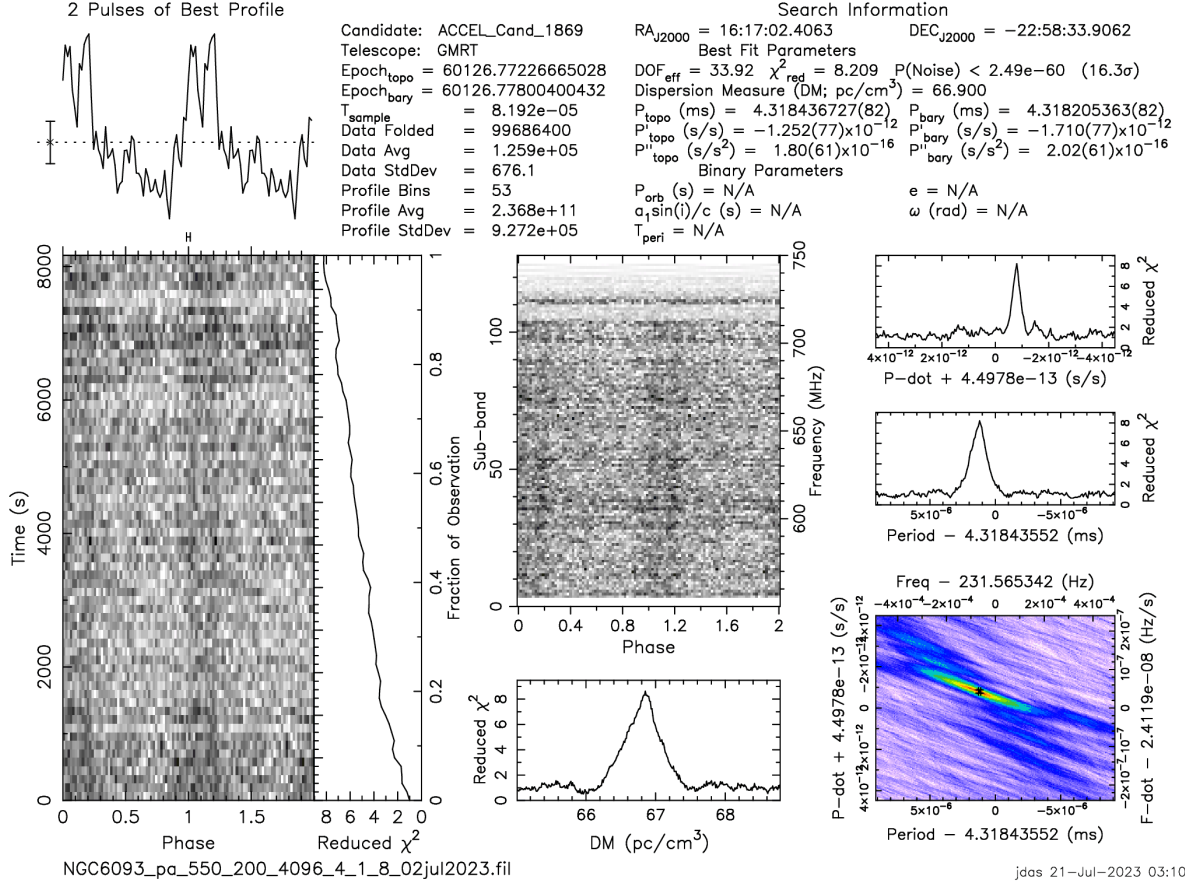


Figure 6. The discovery PRESTO output plot of J1617–2258A, the first MSP of NGC6093. The time versus phase and frequency versus phase output are presented in greyscale in the same figure.

As we can see in Figure 6 and in Figure 8, the MSP has two clear profile components in both frequencies. It also has a faint interpulse. The pulse profile is broader at 400 MHz compared to 650 MHz, where the two components are more distinctly defined. We followed the approach of McKinnon (2014) to determine the scattering timescale and intrinsic profile evolution. In this method, we fit the coherently dedispersed pulse profiles, assuming that all components intrinsically follow a Gaussian distribution and share the same scattering timescale at a given frequency. Additionally, since coherent dedispersion was applied, DM smearing is considered negligible. According to McKinnon (2014), for each profile component, the scattering broadened model can be defined as:

$$f(t, \tau) = A + \frac{S}{2\tau} \exp\left(\frac{\sigma^2}{2\tau^2}\right) \times \exp\left(-\frac{(t - \mu)}{\tau}\right) \times \left(1 + \operatorname{erf}\left[\frac{t - (\mu + \sigma^2/\tau)}{\sigma\sqrt{2}}\right]\right) \quad (7)$$

Here, A is the constant offset, S is the integrated flux density of the component, μ is the mean, σ is the stan-

dard deviation, erf is the error function, and τ is the scattering timescale.

Both Bands' (Band-3 and Band-4) CD pulse profiles' components (except the interpulse) were fitted and components' intrinsic widths and scattering timescale were determined. For each Band, during the fitting of the multiple components, the scattering timescale (τ) was kept fixed, while the components' intrinsic widths (here it's the components' HPBW: $2.355 \times \sigma$) are independent of each other. The fitting was done using the Python package `curve_fit`¹⁵.

In Table 3, we summarise the obtained pulse widths and scattering time scales for this MSP in both the uGMRT Bands. The error we present here is the square root of the diagonal elements of the covariance matrix obtained from the `curve_fit` algorithm to get the independent fitting error of each parameter. As we see in

¹⁵ The package `curve_fit` can be found here: https://docs.scipy.org/doc/scipy/reference/generated/scipy.optimize.curve_fit.html

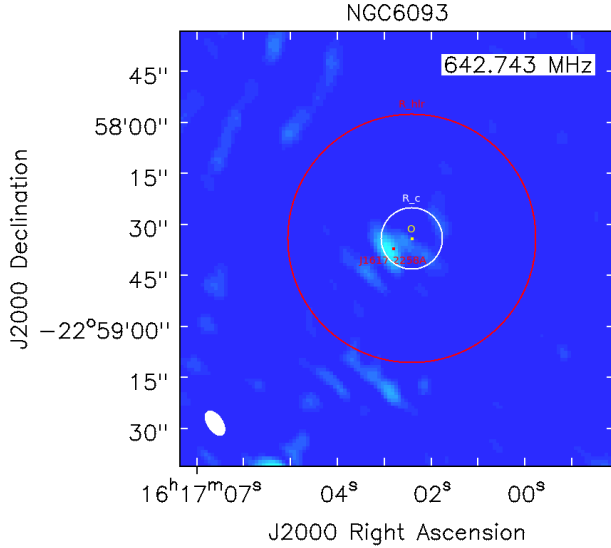


Figure 7. The uGMRT Band-4 ($f_c = 650$ MHz) image of M80 using the CAPTURE pipeline. The image was produced from the simultaneous recording of the beam data during beamforming discovery observation. The yellow and the red circles represent the core radius and the half-light radius of M80 respectively. The point marked with “O” is the GC centre and the position of J1617–2258A is obtained from the timing analysis marked with “A”, which is sitting inside the core radius on the lower-left side.

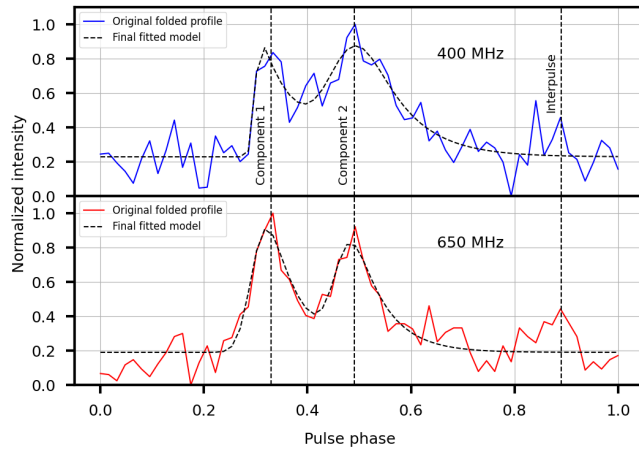


Figure 8. The coherently dedispersed folded profile of the of J1617–2258A for uGMRT Band-3 ($f_c = 650$ MHz) and Band-4 ($f_c = 650$ MHz). For Band-4, the sampling was $10.24 \mu\text{s}$ and for Band-3, the sampling was $40.96 \mu\text{s}$ and both foldings in the plot are downsampled to 64 bins for better visualization. The black line represents the best-fit profile according to Equation 7.

Table 3. The scattering timescale along with the width of both the components obtained from fitting the CD data (data unaffected by intrachannel de-dispersion). We use the convention used in McKinnon (2014), to fit our folded pulse profile. For Band-4, the profile time resolution was $10.24 \mu\text{s}$, and for Band-3, it was $40.96 \mu\text{s}$. The error presented here is obtained from the covariance matrix of the `curve_fit` algorithm.

Frequency (MHz)	Scattering width (ms)	Component number	Intrinsic HPBW (ms)
400	0.328 ± 0.104	1	0.075 ± 0.054
		2	0.416 ± 0.142
650	0.230 ± 0.046	1	0.229 ± 0.037
		2	0.264 ± 0.063

this table (Table 3), for Band-3 ($f_c = 300$ MHz), the obtained values are not as constrained as Band-4 ($f_c = 650$ MHz), due to very low SNR detection of the MSP (as can be seen in Figure 8).

Figure 8 shows the averaged pulse profile for both frequency Bands, each defined by its central frequency (f_c). The profile presented here is obtained after binning the data into 64 intervals for enhanced clarity, with the original fitted model of un-averaged data represented by the dashed curve.

5.4. Timing

Here, we present a detailed discussion of the pulsar’s timing, leading to a phase-coherent timing solution, followed by an analysis of the results obtained from the timing study.

5.4.1. Deriving the orbit

Given the detection with a significant acceleration in the discovery observation, it was clear that it is a binary MSP. To probe the nature of the binary orbit, we followed up on this MSP for seven epochs (including the discovery epoch and one confirmation epoch), with a minimum separation of one day and a maximum separation of one month in two consecutive epochs.

For each epoch, we derived the pulsar period evolution with time and used the timing package FITORBIT¹⁶ to fit a Keplerian model to the temporal variation of spin period. We found that the orbit of J1617–2258A is highly eccentric ($e \sim 0.5374$) and relatively compact relativistic orbit having an orbital period (P_b) ~ 18.94

¹⁶ The GitHub page for the package FITORBIT: <https://github.com/vivekvenkris/fitorbit>

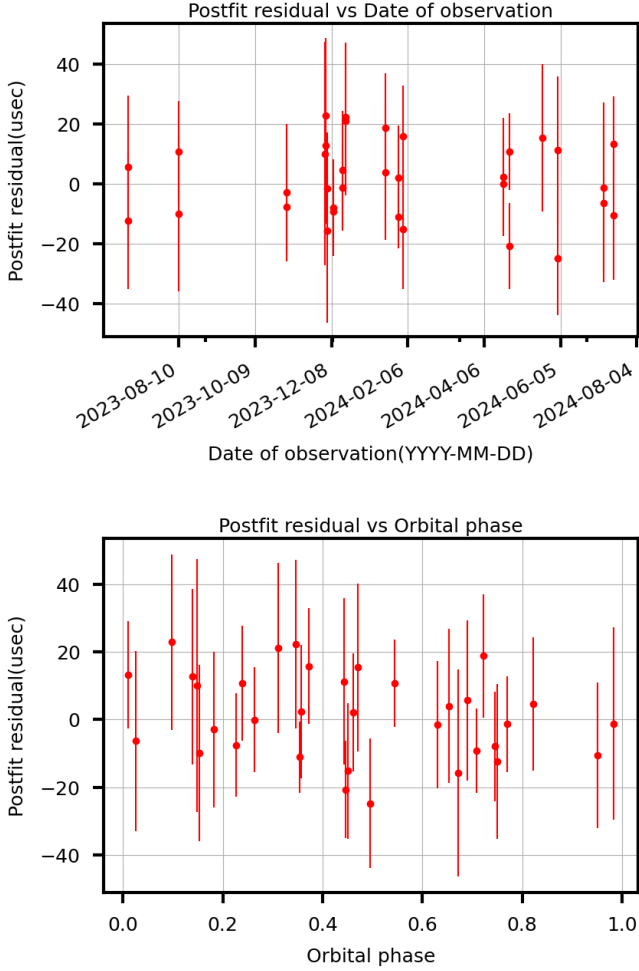


Figure 9. Post-fit timing residual versus epoch (top) and orbital phase (bottom) after achieving the phase-coherent timing solution. The vertical lines with each point represent the rms error of each TOA.

hours, and a projected semi-major axis $x = 0.4642$ s. The mass function of a binary system is given by:

$$f(M_p, M_c) = \frac{(M_p \sin i)^3}{(M_p + M_c)^2} = \frac{4\pi^2 x^3}{T_\odot P_b^2}, \quad (8)$$

where $T_\odot = (\mathcal{G}\mathcal{M}_\odot)^N/c^3 = 4.925490947 \mu\text{s}$ is an exact quantity, the solar mass parameter $(\mathcal{G}\mathcal{M}_\odot)^N$ (Prša et al. 2016) in time units. Assuming $M_p = 1.4 M_\odot$, we obtain a minimum ($i = 90^\circ$) and median ($i = 60^\circ$) companion masses of $0.072 M_\odot$ and $0.084 M_\odot$ respectively.

Although at this stage the timing model was not well constrained, the large eccentricity and relatively compact orbit made this a promising system for the precise measurement of multiple relativistic effects in the orbital motion, which will enable mass measurements in the near future.

5.4.2. Phase connection and timing solution

To achieve phase connection, we conducted biweekly follow-up observations of J1617–2258A using uGMRT Band-4 (550–750 MHz) on 18 occasions, including discovery, confirmation, and follow-up epochs, from July 2023 to August 2024. The timing observations are still ongoing on a monthly cadence. The average detection significance per epoch ranges from 15σ to 30σ depending on the observation duration and phasing efficiency.

We implemented a three-step approach to enhance the precision of the pulse times of arrival (ToAs) measurements and refine the timing solution. We began by using TEMPO¹⁷ to connect the ToAs of nearby epochs, continuing this process until no further unambiguous connections could be established. At this stage, we derived an improved ephemeris, which was then used to re-fold all data, refine pulse profile templates, and re-compute the ToAs. When no more connections could be made, we used DRACULA (Freire & Ridolfi 2018). It is a TEMPO-based software that iteratively determines the unique solution. Finally, with the new parameter file, we again folded all the epochs, generated relatively fewer ToAs to reduce their uncertainties, and did the final iteration of timing to obtain our unique precise timing model, which is presented in Table 4. This uses the DE440 Solar System Ephemeris (Park et al. 2021) to account for the Earth’s motion around the Solar System Barycenter and the “DD” orbital model (Damour & Deruelle 1986) to describe the pulsar’s orbit. Figure 9 represents the post-fit residuals, which are the ToA values minus the prediction of the timing solution in Table 4 for the same rotation.

5.4.3. Position and spin parameters

The precise position of J1617–2258A obtained from the timing (listed in Table 4) coincides with the radio source (as seen in Figure 7) discussed in Section 5.2, confirming its association with J1617–2258A. The pulsar is located $6.44''$ from the cluster centre defined by Vasiliev & Baumgardt (2021). This distance represents about 0.72 core radii, where the core radius is assumed to be $\sim 9''$, see Harris (1996, 2010 edition). At the distance of M80, about 9.8 kpc Vasiliev & Baumgardt (2021), this represents a projected distance of 0.306 pc.

The observed spin period derivative of the pulsar (\dot{P}_{obs}) is the sum of the intrinsic spin period derivative (\dot{P}_{int}) plus contributions from the acceleration of the system in the Galaxy (a_{Gal} , from which we subtract the acceleration of the Solar System in the Galaxy) and in the globular cluster (a_{GC}), both projected along the line of sight to the system and finally the Shklovskii effect

¹⁷ TEMPO GitHub page: <https://github.com/nanograv/tempo>

Table 4. Timing solution of J1617–2258A

Parameters of observation and timing solution	
PSR	J1617–2258A
Reference epoch (MJD)	60166.864788
Start of timing data (MJD)	60126.783
End of timing data (MJD)	60508.571
Number of ToAs	34
Postfit timing residuals, RMS (μ s)	12.137
Solar system ephemeris	DE440
Time units	TDB
Binary model	DD
Measured parameters	
Right Ascension, α (J2000)	16:17:02.821(4)
Declination, δ (J2000)	–22:58:36.8(3)
Spin frequency, f (Hz)	231.572028561(2)
First spin frequency derivative, \dot{f} (Hz s $^{-1}$) ..	–3.3(1) $\times 10^{-15}$
Dispersion measure, DM (pc cm $^{-3}$)	66.812
Orbital period, P_b (d)	0.78914809(7)
Projected semi-major axis, x (lt-s)	0.46421(1)
Eccentricity, e	0.53744(3)
Time of periastron, T_0 (MJD)	60166.84499(2)
Longitude of periastron, ω (degrees)	24.703(9)
Rate of periastron advance, $\dot{\omega}$ (deg year $^{-1}$) ..	0.5851 \pm 0.0149
Derived parameters	
Position offset from GC centre ($''$)	6.444
Position offset from GC centre (core radii) ...	0.72
Spin period, P (ms)	4.318310834921(3)
Spin period derivative, \dot{P} (s s $^{-1}$)	6.1(2) $\times 10^{-20}$
Characteristic age, τ_c (Gyr)	> 0.25
Estimated surface magnetic field, B (10^9 G) .	< 1.1
Mass function, $f(M_p, M_c)$ (M_\odot)	0.00017247(2)
The total mass of the system, M_{tot} (M_\odot) ...	1.67 \pm 0.06
Minimum companion mass, $M_{c,\text{min}}$ (M_\odot)	0.07203(3)
Median companion mass, $M_{c,\text{min}}$ (M_\odot)	0.08361(3)
Maximum pulsar mass, $M_{p,\text{max}}$ (M_\odot)	1.60 \pm 0.06

(Shklovskii 1970), which can be derived from the total proper motion of the system (μ) and its distance (d):

$$\frac{\dot{P}_{\text{obs}}}{P} = \frac{\dot{P}_{\text{int}}}{P} + \frac{a_{\text{Gal}}}{c} + \frac{a_{\text{GC}}}{c} + \frac{\mu^2 d}{c} \quad (9)$$

To calculate a_{Gal} , we have used the Galactic potential model of McMillan (2017), which yields $a_{\text{Gal}} = -0.409 \times 10^{-9} \text{ m s}^{-2}$. To calculate the Shklovskii effect, we have assumed that the proper motion of the pulsar (J1617–2258A) is the same as that of the GC (NGC 6093), which is $\mu_\alpha = -2.934 \pm 0.027 \text{ mas yr}^{-1}$ and $\mu_\delta = -5.578 \pm 0.026 \text{ mas yr}^{-1}$ (Vasiliev & Baumgardt 2021); this results in an apparent acceleration of $a_{\text{Shk}} = \mu^2 d = +0.284 \times 10^{-9} \text{ m s}^{-2}$. Thus the sum of the kinematic contribution from the Galaxy is $-0.122 \times 10^{-9} \text{ m s}^{-2}$. From this, we can derive, for $\dot{P}_{\text{int}} = 0$, an upper limit of the acceleration of the pulsar in the gravitational field of M80 (projected along the

line of sight) as:

$$a_{1,\text{max}} = \frac{\dot{P}_{\text{obs}}}{P} c - a_{\text{Gal}} - a_{\text{Shk}} = +4.35 \times 10^{-9} \text{ m s}^{-2}. \quad (10)$$

To model the gravitational field of M80, we use the analytical model described by Freire et al. (2005), where we use a velocity dispersion in the core of 12.4 km s^{-1} (Harris 1996, 2010 edition). For the line of sight of the pulsar, this model predicts a maximum/minimum cluster acceleration of $a_{\text{GC}} = \pm 14.75 \times 10^{-9} \text{ m s}^{-2}$, which is significantly larger than $a_{1,\text{max}}$ of the pulsar; this means that the value of $a_{1,\text{max}}$ is well within the range of accelerations predicted by our mass model for M80. Assuming the minimum possible cluster acceleration, we obtain an absolute upper limit of $\dot{P}_{\text{int}} < 2.75 \times 10^{-19}$. From this value, the limits on characteristic age (τ), and surface magnetic field strength (B) can be estimated using:

$$\tau_c = P/2\dot{P}, \quad B = 3.2 \times 10^{19} \left(P\dot{P} \right)^{1/2}, \quad (11)$$

from which we obtain, $\tau_c > 0.25 \text{ Gyr}$, and $B < 1.1 \times 10^9 \text{ G}$. These values are not very constraining, but they are consistent with typical values obtained for MSPs in the Galactic disk. Much improved values will be obtained when the orbital period derivative of the system becomes measurable (see e.g., discussion in Freire et al. (2017)).

5.5. Binary characteristics

In this section, we discuss the binary characteristics of J1617–2258A, the unique compact eccentric orbit and its companion type.

5.5.1. The compact eccentric orbit of J1617–2258A

During the evolution of binary MSPs, as the orbit gets compact due to close interaction with its binary companion, the orbit gets circularized losing its eccentricity due to tidal effects. With companion mass towards lower values, it's harder for a compact orbit to maintain its ellipticity in a compact orbit. Figure 11 clearly shows that all the highly elliptic orbits either have a higher companion mass, a very wide orbit, or both. Interestingly in our case, this MSP doesn't follow this trend. This MSP J1617–2258A is in a ~ 18.94 hours compact but highly eccentric ($e \sim 0.54$) binary orbit, which is quite uncommon. In Figure 11 the unique position of this MSP is visible, where there are only 4 MSPs (3 are from Globular Clusters) orbits more compact and more eccentric than this orbit but all of them have a median companion mass higher than J1617–2258A's median companion mass.

The reason for J1617–2258A’s highly eccentric compact orbit could be interaction with a distant star changing the ellipticity of the orbit, or close flybys of stars in past (e.g. [Phinney 1992](#)).

5.5.2. Rate of advance of periastron

With more than one year of timing baseline, this highly eccentric compact orbit allowed us to detect one post-Keplerian (PK) parameter, the rate of advance of periastron ($\dot{\omega}$) in our timing with sufficient detection significance. If this is purely relativistic, then in general relativity (GR), this is related to the total mass of the system by ($M_{\text{tot}} = M_{\text{p}} + M_{\text{c}}$):

$$\dot{\omega} = 3T_{\odot}^{2/3} \left(\frac{P_{\text{b}}}{2\pi} \right)^{-5/3} \frac{(M_{\text{p}} + M_{\text{c}})^{2/3}}{1 - e^2} \quad (12)$$

Our measurement of $\dot{\omega}$ results in $M_{\text{tot}} = 1.67 \pm 0.06 M_{\odot}$. In [Fig. 10](#), this constraint and its $1\text{-}\sigma$ uncertainty are indicated by the solid red lines.

If we combine the nominal value of the total mass with the mass function equation (given by [eq. 10](#), which excludes the grey area in the right plot of [Fig. 10](#)), we obtain for $i = 90^\circ$ a minimum companion mass of $0.072 M_{\odot}$ and a maximum pulsar mass of $1.60 M_{\odot}$. The previous assumption of $M_{\text{p}} = 1.4 M_{\odot}$ would result in $M_{\text{c}} \sim 0.27 \pm 0.06 M_{\odot}$ and an improbably low orbital inclination of $i = 16.6 \pm 2.9^\circ$.

5.5.3. Detailed mass estimates

Given the uncertainties of $\dot{\omega}$, the previous mass estimates are only approximate. To better quantify the masses and their uncertainties given the constraints of the timing – including the constraints from the lack of measurement of the Shapiro delay, and any other relativistic effects that might be present in the timing with low significance – we have made a Bayesian χ^2 map. This samples $\cos i$ and M_{tot} uniformly. For each point in this grid, we calculate M_{c} and then include the values of M_{tot} and M_{c} in a DDGR ([Damour & Deruelle 1986](#)) timing solution, where they are kept fixed. This type of orbital model assumes the validity of GR, and in a self-consistent way takes into account all relativistic constraints that might be present in the timing. We then use TEMPO to obtain the optimal solution for those values, recording the value of χ^2 . This is then converted into a 2-D probability density function (pdf) using the Bayesian method of [Splaver et al. \(2002\)](#). We then project this pdf into the $\cos i - M_{\text{c}}$ and $M_{\text{p}} - M_{\text{c}}$ spaces, and from these we derive the 1-D pdfs for M_{tot} , M_{p} , M_{c} and $\cos i$.

These 2-D and 1-D pdfs are depicted in [Fig. 10](#). In the main panels, the pdfs are depicted by contours that

include 68.3%, 95.4% and 99.7% of the 2-D pdf in each panel. In the marginal panels, we depict the 1-D pdfs for $\cos i$, M_{p} and M_{c} .

The medians and $\pm 1\text{-}\sigma$ percentiles of these pdfs are: $M_{\text{tot}} = 1.672 \pm 0.063 M_{\odot}$, $M_{\text{p}} = 1.567_{-0.080}^{+0.060} M_{\odot}$ and $M_{\text{c}} = 0.086_{-0.012}^{+0.056} M_{\odot}$.

For $\cos i$, we see that the pdf is nearly flat, as in our assumed prior. This means that no other relativistic effects are detected and that at the moment the individual masses cannot be estimated, other than via the statistical assumption of a flat distribution of $\cos i$.

5.5.4. The companion and binary type

During timing observation, we roughly sampled every part of the orbit ([Figure 9](#)) and for every observation, this MSP was detected at about the expected SNR and no eclipsing phenomenon has been observed. In most cases, spider MSPs (redbacks and black widows) show eclipsing due to the interaction of the pulsar pulse with its non-degenerate companion outflows ([Yan et al. 2021](#); [Kumari et al. 2024](#)). If this MSP system is a spider system then either the eclipsing is covering a very small part of the orbital phase and the region remained unsampled till now or the eclipsing could be frequency dependent, but for that fine sampling of the orbital phase and observation in different frequency except 550–750 MHz is needed to confirm if it is a spider MSP system.

Another possibility is that the system is not a spider system but rather a neutron star-white-dwarf (NS–WD) binary system. For MSP with a Population-I WD companion, according to [Tauris & Savonije \(1999\)](#)’s $P_{\text{b}} - M_{\text{c}}$ correlation, for compact orbit ($P_{\text{b}} \sim 1$ days) we can write:

$$\frac{M_{\text{c}}}{M_{\odot}} = \left(\frac{P_{\text{b}}}{b} \right)^{1/a} + c \quad (13)$$

Where, P_{b} in days, $a = 4.50$, $b = 1.2 \times 10^5$, and $c = 0.12$. Putting our P_{b} value into [Equation 13](#), we get our $M_{\text{c}} = 0.19 M_{\odot}$, which would imply $M_{\text{p}} = 1.48 \pm 0.6 M_{\odot}$ and $i \sim 24^\circ$. If this low orbital inclination is correct, measuring the Shapiro delay in this system will not be possible, which agrees with our previous analysis.

However, in the Galaxy, most MSP-WD systems have very low eccentricities, of the order of 10^{-6} to 10^{-4} . Assuming J1617–2258A is an NS-WD binary, then the large eccentricity of J1617–2258A is likely caused by interactions with other stars in the GC, which will increase its eccentricity, as mentioned earlier in [Section 5.5.1](#).

The large eccentricity means that we cannot exclude another possibility: the system could be the result of an exchange encounter. However, in exchanges that occur, the new companion will likely be significantly more massive than the initial donor ([Freire et al. 2004](#); [Camilo](#)

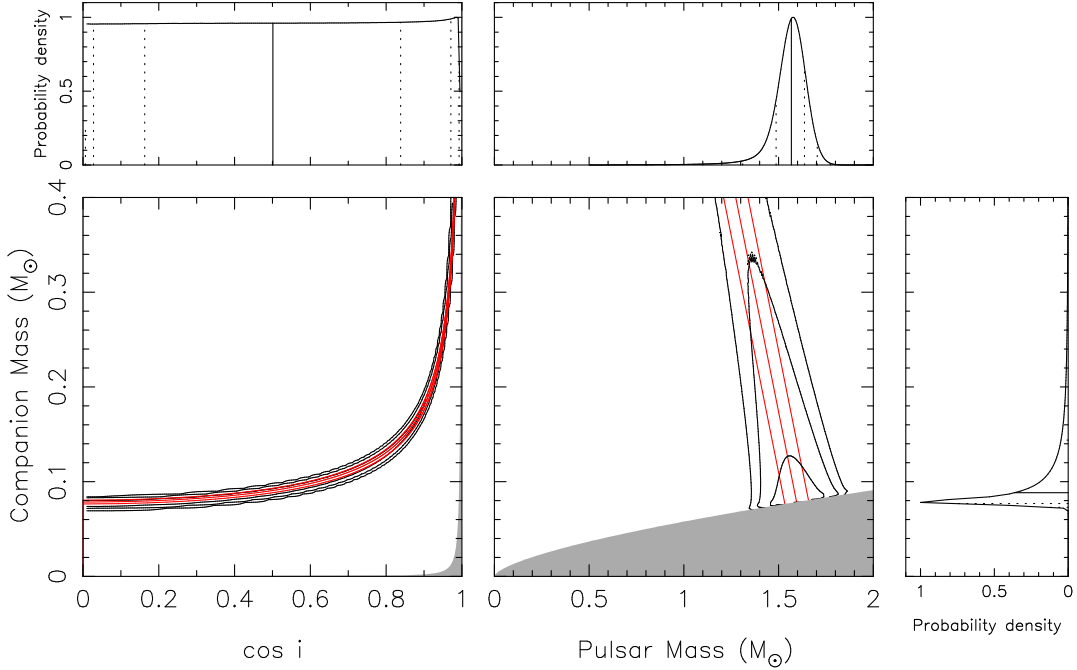


Figure 10. Mass-mass diagram for J1617–2258A. *Main left panel:* $\cos i - M_c$ space. The grey area is excluded by the requirement that $M_p > 0$. *Main right panel:* $M_p - M_c$ space. The grey area is excluded by the requirement that $\sin i \leq 0$. The mass constraints from the measurement of $\dot{\omega}$ are depicted in red. The solid black contours include 68.3%, 95.4% and 99.7% of all probability in the pdfs in each panel. *Side panels, top left:* 1-D pdf for $\cos i$, *Top right:* 1-D pdf for M_p , *right-side panel:* 1-D pdf for M_c , the solid and dotted lines depict their medians and 1, 2 and 3- σ equivalent percentiles.

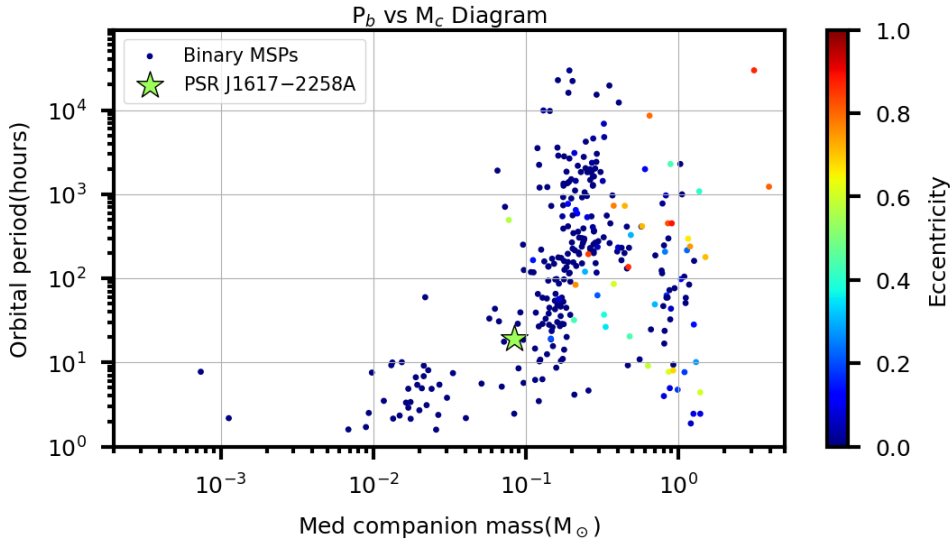


Figure 11. The plot of the orbital period versus median companion mass for all the binary MSPs detected till now along with GCGPS's J1617–2258A. All the binary MSP data was taken from the ATNF Pulsar catalogue (Manchester et al. 2005). The additional axis is the eccentricity of each system represented as the colour of each dot and the color bar represents the eccentricity range. We can see that the highly eccentric orbits are either very wide or have a high mass companion or both, while the newly discovered GC MSP J1617–2258A, having a compact orbit and a companion with low median mass is quite eccentric and sitting in a unique spot in the plot with high eccentricity.

& Rasio 2005). The relatively low companion mass of J1617–2258A is compatible with its current companion being the white dwarf remnant of the star that recycled the pulsar.

We tried to detect the companion in the HST archival data¹⁸ of NGC 6093 using different filters at the position obtained from the timing of the MSP. We couldn't conclusively determine any possible companion and its type from the optical study. Considering all the possibilities, the most likely scenario is that this system is a neutron-star-helium-white-dwarf (NS-He-WD) system, where the large eccentricity is likely caused by interactions with other stars in the GC, or close flybys of stars in the past. Further study is needed to conclude its companion type.

6. SUMMARY

This paper discusses the Globular Clusters GMRT Pulsar Search (GCGPS) survey. GCGPS has recently started and is currently searching for MSPs in GCs. This survey is designed to search for GC pulsars in the low-frequency range (300–750 MHz). The target selection criteria and observation strategy are optimized to increase discovery potential. GCGPS survey exploits uGMRT's Y-shaped array to form two beams with dif-

ferent baseline lengths to optimize sky coverage along with beam sensitivity.

We present the discovery of the first MSP in the globular cluster NGC6093 (M80). We localise the MSP from imaging of the field as well as from timing solutions at sub-arc-sec precision. The timing of the MSP revealed that it is in a highly eccentric ($e \sim 0.54$) compact ($P_b \sim 18.94$ h) relativistic binary. Measurement of one PK parameter (advance of periastron, $\dot{\omega}$) leads to measurement of the total mass of the system ($M_{\text{tot}} = 1.67 \pm 0.06 M_{\odot}$), this and the mass function imply $M_c \geq 0.072 M_{\odot}$ and $M_p \leq 1.60 M_{\odot}$. The limit on the companion mass is consistent with it being a He WD whose progenitor spun up the pulsar, although we cannot exclude the possibility that the system might have formed in an exchange interaction. There are only four such systems that are more compact and eccentric than this system, but all have a higher median companion mass than this system.

We acknowledge the support of the Department of Atomic Energy, Government of India, under project No. 12-R&D-TFR5.02-0700. The GMRT is run by the National Center for Radio Astrophysics of the Tata Institute of Fundamental Research, India. We thank the uGMRT operators for their coordinated effort in conducting the GCGPS survey observations.

REFERENCES

- Abbate, F., Ridolfi, A., Barr, E. D., et al. 2022, MNRAS, 513, 2292, doi: [10.1093/mnras/stac1041](https://doi.org/10.1093/mnras/stac1041)
- Abbate, F., Ridolfi, A., Freire, P. C. C., et al. 2023, A&A, 680, A47, doi: [10.1051/0004-6361/202347725](https://doi.org/10.1051/0004-6361/202347725)
- Abdo, A. A., Ackermann, M., Ajello, M., et al. 2010, A&A, 524, A75, doi: [10.1051/0004-6361/201014458](https://doi.org/10.1051/0004-6361/201014458)
- Bahramian, A., Heinke, C. O., Sivakoff, G. R., & Gladstone, J. C. 2013, ApJ, 766, 136, doi: [10.1088/0004-637X/766/2/136](https://doi.org/10.1088/0004-637X/766/2/136)
- Barr, E. D., Dutta, A., Freire, P. C. C., et al. 2024, Science, 383, 275, doi: [10.1126/science.adg3005](https://doi.org/10.1126/science.adg3005)
- Becker, W., & Trümper, J. 1999, A&A, 341, 803, doi: [10.48550/arXiv.astro-ph/9806381](https://doi.org/10.48550/arXiv.astro-ph/9806381)
- Bhat, N. D. R., Cordes, J. M., Camilo, F., Nice, D. J., & Lorimer, D. R. 2004, ApJ, 605, 759, doi: [10.1086/382680](https://doi.org/10.1086/382680)
- Bhattacharyya, B., Cooper, S., Malenta, M., et al. 2016, ApJ, 817, 130, doi: [10.3847/0004-637X/817/2/130](https://doi.org/10.3847/0004-637X/817/2/130)
- Bhattacharyya, B., Roy, J., Stappers, B. W., et al. 2019, ApJ, 881, 59, doi: [10.3847/1538-4357/ab2bf3](https://doi.org/10.3847/1538-4357/ab2bf3)
- Bogdanov, S., van den Berg, M., Servillat, M., et al. 2011, ApJ, 730, 81, doi: [10.1088/0004-637X/730/2/81](https://doi.org/10.1088/0004-637X/730/2/81)
- Camilo, F., Lorimer, D. R., Freire, P., Lyne, A. G., & Manchester, R. N. 2000, ApJ, 535, 975, doi: [10.1086/308859](https://doi.org/10.1086/308859)
- Camilo, F., & Rasio, F. A. 2005, in Astronomical Society of the Pacific Conference Series, Vol. 328, Binary Radio Pulsars, ed. F. A. Rasio & I. H. Stairs, 147, doi: [10.48550/arXiv.astro-ph/0501226](https://doi.org/10.48550/arXiv.astro-ph/0501226)
- Chen, J., Cadelano, M., Pallanca, C., et al. 2023, ApJ, 948, 84, doi: [10.3847/1538-4357/acc583](https://doi.org/10.3847/1538-4357/acc583)
- Cordes, J. M., & Lazio, T. J. W. 2002, arXiv e-prints, astro, doi: [10.48550/arXiv.astro-ph/0207156](https://doi.org/10.48550/arXiv.astro-ph/0207156)
- Corongiu, A., Ridolfi, A., Abbate, F., et al. 2024, ApJ, 972, 198, doi: [10.3847/1538-4357/ad5e74](https://doi.org/10.3847/1538-4357/ad5e74)
- D'Amico, N., Possenti, A., Manchester, R. N., et al. 2003, in Astronomical Society of the Pacific Conference Series, Vol. 302, Radio Pulsars, ed. M. Bailes, D. J. Nice, & S. E. Thorsett, 375

¹⁸ HST GC archival data site: <https://archive.stsci.edu/prepds/hugs/>

- Damour, T., & Deruelle, N. 1986, *Annales de L'Institut Henri Poincare Section (A) Physique Theorique*, 44, 263
- DeCesar, M. E., Ransom, S. M., Kaplan, D. L., Ray, P. S., & Geller, A. M. 2015, *ApJL*, 807, L23, doi: [10.1088/2041-8205/807/2/L23](https://doi.org/10.1088/2041-8205/807/2/L23)
- Dewey, R. J., Taylor, J. H., Weisberg, J. M., & Stokes, G. H. 1985, *ApJL*, 294, L25, doi: [10.1086/184502](https://doi.org/10.1086/184502)
- Douglas, A., Padmanabh, P. V., Ransom, S. M., et al. 2022, *ApJ*, 927, 126, doi: [10.3847/1538-4357/ac4744](https://doi.org/10.3847/1538-4357/ac4744)
- Freire, P. C., Gupta, Y., Ransom, S. M., & Ishwara-Chandra, C. H. 2004, *ApJL*, 606, L53, doi: [10.1086/421085](https://doi.org/10.1086/421085)
- Freire, P. C. C., Hessels, J. W. T., Nice, D. J., et al. 2005, *ApJ*, 621, 959, doi: [10.1086/427748](https://doi.org/10.1086/427748)
- Freire, P. C. C., Ransom, S. M., Bégin, S., et al. 2008, *ApJ*, 675, 670, doi: [10.1086/526338](https://doi.org/10.1086/526338)
- Freire, P. C. C., & Ridolfi, A. 2018, *MNRAS*, 476, 4794, doi: [10.1093/mnras/sty524](https://doi.org/10.1093/mnras/sty524)
- Freire, P. C. C., & Wex, N. 2024, *Living Reviews in Relativity*, 27, 5, doi: [10.1007/s41114-024-00051-y](https://doi.org/10.1007/s41114-024-00051-y)
- Freire, P. C. C., Abdo, A. A., Ajello, M., et al. 2011, *Science*, 334, 1107, doi: [10.1126/science.1207141](https://doi.org/10.1126/science.1207141)
- Freire, P. C. C., Ridolfi, A., Kramer, M., et al. 2017, *MNRAS*, 471, 857, doi: [10.1093/mnras/stx1533](https://doi.org/10.1093/mnras/stx1533)
- Gautam, T., Ridolfi, A., Freire, P. C. C., et al. 2022, *A&A*, 664, A54, doi: [10.1051/0004-6361/202243062](https://doi.org/10.1051/0004-6361/202243062)
- Gupta, Y., Ajithkumar, B., Kale, H. S., et al. 2017, *Current Science*, 113, 707, doi: [10.18520/cs/v113/i04/707-714](https://doi.org/10.18520/cs/v113/i04/707-714)
- Hankins, T. H. 1971, *ApJ*, 169, 487, doi: [10.1086/151164](https://doi.org/10.1086/151164)
- Harris, W. E. 1996, *AJ*, 112, 1487, doi: [10.1086/118116](https://doi.org/10.1086/118116)
- He, Q., & Shi, X. 2024, *MNRAS*, 527, 5183, doi: [10.1093/mnras/stad3561](https://doi.org/10.1093/mnras/stad3561)
- Hessels, J. W. T., Ransom, S. M., Stairs, I. H., Kaspi, V. M., & Freire, P. C. C. 2007, *ApJ*, 670, 363, doi: [10.1086/521780](https://doi.org/10.1086/521780)
- Johnson, T. J., Guillemot, L., Kerr, M., et al. 2013, *ApJ*, 778, 106, doi: [10.1088/0004-637X/778/2/106](https://doi.org/10.1088/0004-637X/778/2/106)
- Kale, R., & Ishwara-Chandra, C. H. 2021, *Experimental Astronomy*, 51, 95, doi: [10.1007/s10686-020-09677-6](https://doi.org/10.1007/s10686-020-09677-6)
- Kudale, S., Roy, J., Chengalur, J. N., Sharma, S., & Kumari, S. 2024, *ApJ*, 972, 61, doi: [10.3847/1538-4357/ad6315](https://doi.org/10.3847/1538-4357/ad6315)
- Kumari, S., Bhattacharyya, B., Sharan, R., et al. 2024, *ApJ*, 973, 19, doi: [10.3847/1538-4357/ad6145](https://doi.org/10.3847/1538-4357/ad6145)
- Li, B., Zhang, L.-y., Yao, J., et al. 2024, *ApJ*, 972, 43, doi: [10.3847/1538-4357/ad5a82](https://doi.org/10.3847/1538-4357/ad5a82)
- Lian, Y., Pan, Z., Zhang, H., et al. 2023, *ApJL*, 951, L37, doi: [10.3847/2041-8213/acdee7](https://doi.org/10.3847/2041-8213/acdee7)
- Lian, Y., Freire, P. C. C., Cao, S., et al. 2025, arXiv e-prints, arXiv:2502.02042, doi: [10.48550/arXiv.2502.02042](https://doi.org/10.48550/arXiv.2502.02042)
- Lorimer, D. R., & Kramer, M. 2004, *Handbook of Pulsar Astronomy*, Vol. 4
- Lynch, R. S., Freire, P. C. C., Ransom, S. M., & Jacoby, B. A. 2012, *ApJ*, 745, 109, doi: [10.1088/0004-637X/745/2/109](https://doi.org/10.1088/0004-637X/745/2/109)
- Lynch, R. S., Ransom, S. M., Freire, P. C. C., & Stairs, I. H. 2011, *ApJ*, 734, 89, doi: [10.1088/0004-637X/734/2/89](https://doi.org/10.1088/0004-637X/734/2/89)
- Manchester, R. N., Hobbs, G. B., Teoh, A., & Hobbs, M. 2005, *AJ*, 129, 1993, doi: [10.1086/428488](https://doi.org/10.1086/428488)
- McKinnon, M. M. 2014, *PASP*, 126, 476, doi: [10.1086/676975](https://doi.org/10.1086/676975)
- McMillan, P. J. 2017, *MNRAS*, 465, 76, doi: [10.1093/mnras/stw2759](https://doi.org/10.1093/mnras/stw2759)
- Padmanabh, P. V., Ransom, S. M., Freire, P. C. C., et al. 2024, *A&A*, 686, A166, doi: [10.1051/0004-6361/202449303](https://doi.org/10.1051/0004-6361/202449303)
- Pan, Z., Qian, L., Ma, X., et al. 2021a, *ApJL*, 915, L28, doi: [10.3847/2041-8213/ac0bbd](https://doi.org/10.3847/2041-8213/ac0bbd)
- Pan, Z., Ma, X.-Y., Qian, L., et al. 2021b, *Research in Astronomy and Astrophysics*, 21, 143, doi: [10.1088/1674-4527/21/6/143](https://doi.org/10.1088/1674-4527/21/6/143)
- Park, R. S., Folkner, W. M., Williams, J. G., & Boggs, D. H. 2021, *AJ*, 161, 105, doi: [10.3847/1538-3881/abd414](https://doi.org/10.3847/1538-3881/abd414)
- Phinney, E. S. 1992, *Philosophical Transactions of the Royal Society of London Series A*, 341, 39, doi: [10.1098/rsta.1992.0084](https://doi.org/10.1098/rsta.1992.0084)
- Pooley, D., Lewin, W. H. G., Anderson, S. F., et al. 2003, *ApJL*, 591, L131, doi: [10.1086/377074](https://doi.org/10.1086/377074)
- Possenti, A., D'Amico, N., Corongiu, A., et al. 2005, in *Astronomical Society of the Pacific Conference Series*, Vol. 328, *Binary Radio Pulsars*, ed. F. A. Rasio & I. H. Stairs, 189
- Possenti, A., D'Amico, N., Manchester, R. N., et al. 2001, arXiv e-prints, astro, doi: [10.48550/arXiv.astro-ph/0108343](https://doi.org/10.48550/arXiv.astro-ph/0108343)
- Prša, A., Harmanec, P., Torres, G., et al. 2016, *AJ*, 152, 41, doi: [10.3847/0004-6256/152/2/41](https://doi.org/10.3847/0004-6256/152/2/41)
- Ransom, S. M., Hessels, J. W. T., Stairs, I. H., et al. 2005, *Science*, 307, 892, doi: [10.1126/science.1108632](https://doi.org/10.1126/science.1108632)
- Ransom, S. M., Stairs, I. H., Backer, D. C., et al. 2004, *ApJ*, 604, 328, doi: [10.1086/381730](https://doi.org/10.1086/381730)
- Reddy, S. H., Kudale, S., Gokhale, U., et al. 2017, *Journal of Astronomical Instrumentation*, 6, 1641011, doi: [10.1142/S2251171716410117](https://doi.org/10.1142/S2251171716410117)
- Ridolfi, A., Gautam, T., Freire, P. C. C., et al. 2021, *MNRAS*, 504, 1407, doi: [10.1093/mnras/stab790](https://doi.org/10.1093/mnras/stab790)

- Ridolfi, A., Freire, P. C. C., Gautam, T., et al. 2022a, *A&A*, 664, A27, doi: [10.1051/0004-6361/202143006](https://doi.org/10.1051/0004-6361/202143006)
- . 2022b, *A&A*, 664, A27, doi: [10.1051/0004-6361/202143006](https://doi.org/10.1051/0004-6361/202143006)
- Sarazin, C. L., Kundu, A., Irwin, J. A., et al. 2003, *ApJ*, 595, 743, doi: [10.1086/377467](https://doi.org/10.1086/377467)
- Shklovskii, I. S. 1970, *Soviet Ast.*, 13, 562
- Singleton, J., DeCesar, M., Dai, S., et al. 2024, arXiv e-prints, arXiv:2412.11271, doi: [10.48550/arXiv.2412.11271](https://doi.org/10.48550/arXiv.2412.11271)
- Splaver, E. M., Nice, D. J., Arzoumanian, Z., et al. 2002, *ApJ*, 581, 509, doi: [10.1086/344202](https://doi.org/10.1086/344202)
- Swarup, G., Ananthakrishnan, S., Kapahi, V. K., et al. 1991, *Current Science*, 60, 95. <http://www.jstor.org/stable/24094934>
- Tam, P.-H. T., Hui, C. Y., & Kong, A. K. H. 2016, *Journal of Astronomy and Space Sciences*, 33, 1, doi: [10.5140/JASS.2016.33.1.1](https://doi.org/10.5140/JASS.2016.33.1.1)
- Tam, P. H. T., Kong, A. K. H., Hui, C. Y., et al. 2011, *ApJ*, 729, 90, doi: [10.1088/0004-637X/729/2/90](https://doi.org/10.1088/0004-637X/729/2/90)
- Tauris, T. M., & Savonije, G. J. 1999, *A&A*, 350, 928, doi: [10.48550/arXiv.astro-ph/9909147](https://doi.org/10.48550/arXiv.astro-ph/9909147)
- Tauris, T. M., & van den Heuvel, E. P. J. 2023, *Physics of Binary Star Evolution. From Stars to X-ray Binaries and Gravitational Wave Sources*, doi: [10.48550/arXiv.2305.09388](https://doi.org/10.48550/arXiv.2305.09388)
- Vasiliev, E., & Baumgardt, H. 2021, *MNRAS*, 505, 5978, doi: [10.1093/mnras/stab1475](https://doi.org/10.1093/mnras/stab1475)
- Verbunt, F., & Freire, P. C. C. 2014, *A&A*, 561, A11, doi: [10.1051/0004-6361/201321177](https://doi.org/10.1051/0004-6361/201321177)
- Verbunt, F., & Hut, P. 1987, in *IAU Symposium*, Vol. 125, *The Origin and Evolution of Neutron Stars*, ed. D. J. Helfand & J. H. Huang, 187
- Vleeschower, L., Corongiu, A., Stappers, B. W., et al. 2024, *MNRAS*, 530, 1436, doi: [10.1093/mnras/stae816](https://doi.org/10.1093/mnras/stae816)
- Wang, L., Peng, B., Stappers, B. W., et al. 2020, *ApJ*, 892, 43, doi: [10.3847/1538-4357/ab76cc](https://doi.org/10.3847/1538-4357/ab76cc)
- Webb, N. A., Wheatley, P. J., & Barret, D. 2006, *A&A*, 445, 155, doi: [10.1051/0004-6361:20053010](https://doi.org/10.1051/0004-6361:20053010)
- Wu, Y., Pan, Z., Qian, L., et al. 2024, *ApJL*, 974, L23, doi: [10.3847/2041-8213/ad7b9e](https://doi.org/10.3847/2041-8213/ad7b9e)
- Yan, Z., Pan, Z.-c., Ransom, S. M., et al. 2021, *ApJ*, 921, 120, doi: [10.3847/1538-4357/ac25eb](https://doi.org/10.3847/1538-4357/ac25eb)
- Yao, J. M., Manchester, R. N., & Wang, N. 2017, *ApJ*, 835, 29, doi: [10.3847/1538-4357/835/1/29](https://doi.org/10.3847/1538-4357/835/1/29)
- Yin, D., Zhang, L.-y., Qian, L., et al. 2024, *ApJL*, 969, L7, doi: [10.3847/2041-8213/ad534e](https://doi.org/10.3847/2041-8213/ad534e)
- Zhang, L., & Cheng, K. S. 2003, *A&A*, 398, 639, doi: [10.1051/0004-6361:20021570](https://doi.org/10.1051/0004-6361:20021570)
- Zhang, L., Freire, P. C. C., Ridolfi, A., et al. 2023, *ApJS*, 269, 56, doi: [10.3847/1538-4365/acfb03](https://doi.org/10.3847/1538-4365/acfb03)
- Zhang, P., Xing, Y., & Wang, Z. 2022, *ApJL*, 935, L36, doi: [10.3847/2041-8213/ac88bf](https://doi.org/10.3847/2041-8213/ac88bf)
- Zhou, D., Wang, P., Li, D., et al. 2024, *Science China Physics, Mechanics, and Astronomy*, 67, 269512, doi: [10.1007/s11433-023-2362-x](https://doi.org/10.1007/s11433-023-2362-x)